Influence of the uncertainty of elastic constants on the modelling of ultrasound propagation through multi-pass austenitic welds. Impact on non-destructive testing

Cécile Gueudré, Jean Mailhé, Marie-Aude Ploix, Gilles Corneloup, Bertrand Chassignole

Title

Influence of the uncertainty of elastic constants on the modelling of ultrasound propagation through multi-pass austenitic welds. Impact on Non-Destructive Testing

Authors' names and affiliations

Cécile GUEUDRE[1], Jean MAILHE[1], Marie-Aude PLOIX[1], Gilles CORNELOUP[1], Bertrand CHASSIGNOLE[2]

[1] Aix Marseille Université, CNRS, Centrale Marseille,
LMA, Laboratoire de Mécanique et d'Acoustique,
Marseille, France

[2] EDF Lab, les Renardières,
Département Matériaux et Mécanique des Composants,
Moret sur Loing, France

*Corresponding author
Phone number: +33 (0) 4 42 93 90 34
E-mail address: cecile.gueudre@univ-amu.fr
Postal Address: Laboratoire de Mécanique et d'Acoustique, CNRS - UMR 7031
Aix Marseille Université, IUT GMP
413 Avenue Gaston Berger
13 625 Aix en Provence Cedex1

Abstract

Ultrasonic NDT is used on austenitic stainless steel welds in PWRs. Propagation modelling facilitates diagnostic concerning the detection of a possible defect if a realistic description of those heterogeneous anisotropic welds is introduced. A macrography, or MINA model, coupled with the ultrasonic code ATHENA, reproduces the deviations and divisions of the beam. In certain cases, some discrepancies between theory and experimentation are observed, and this study shows that they can be partly attributed to the uncertainty of the elastic constants Cij, complex to evaluate and measured on specimens sometimes little representative of the welded metal. We chose the seismogram as descriptor of phenomena to keep a maximum amount of information, to generate sensitivity and uncertainty maps. The zones sensitive (or not) to the variations of each Cij are revealed, helping in the choice of the test configurations. The analytical uncertainty propagation method is used to quantify the influence of Cij variability on the propagation simulation. The deviation in position and in time of flight of a classical ultrasonic test (NDT) is clearly shown.

Keywords

Ultrasonics, weld, modelling, uncertainty, elasticity constants

1. INTRODUCTION

The primary circuit in pressurized water reactors includes numerous components, such as the vessel, the steam generator, the primary pumps, the pressurizer, interconnected by a piping system conveying high pressure, high temperature water. Most of these components are made of austenitic stainless steel, as it exhibits excellent corrosion resistance and very good mechanical strength at high temperature. Non-destructive testing aims at detecting potential defects in the numerous multi-pass welds present in the primary circuit and at characterizing them (position and dimensions), so that their severity can be assessed.

Very often, radiographic testing cannot be used for the detection of welding defects, in view of the great thicknesses to check, their sometimes large variations, the limited traceability of some planar defects, and because it may sometimes be impossible to position the film behind the part. Moreover, radiographic testing requires important radioprotection constraints. Ultrasonic testing makes it possible to detect and characterize defects whatever their orientation, but the results may be problematic to interpret, especially for these complex thick welds. A realistic prediction of the microstructure should provide valuable insight into ultrasonic propagation through those complex structures and thereby allow a better controllability.

An austenitic weld is anisotropic and heterogeneous: there is together elongation of the grains parallel to the lines of heat dissipation (morphological texture), along the preferential crystallographic axis <100> of the face-centered cubic single crystal (crystallographic texture), and evolution of the grain orientation in the welded volume. The non-destructive ultrasonic testing of such welds reveals phenomena of deviation and division of the ultrasound beam generated by the structure, as well as attenuation and

structure noise [1,2]. An idea to eliminate the cause of the ultrasonic testing complications is to try to master the size and growth direction of columnar grains by modifications of the welding process (application of electromagnetic fields, pulse TIG arc welding, …) [3]. Other current work aim at use phased array technology [7,20,28–30] associated with particular methods of acquisition and post-processing (Full Matrix Capture [31], Total Focusing Method [7], DORT method based on the principle of time reversal [32] and topological energy method [33]) in order to improve detection in welds. Another way chosen here consists in performing simulation of the ultrasonic propagation with the aim of a better understanding of the propagation phenomena.

Numerous simulation codes of ultrasonic propagation are available in the literature to address the problem of ultrasonic testing of polycrystalline metals with both anisotropic and heterogeneous structures. Many of them are based on ray-tracing methods [4–7] because they are less expensive in computation time than finite element methods (FEM). CIVA, developed by the CEA, proposes field computation and defect echo calculation modules based on semi-analytical formulations [8]. A hybrid model of CIVA named ECHO is based on a coupling of the CIVA model and the spectral finite element code ONDOMATIC [9].

ATHENA code used here and developed by EDF is a finite element code that solves the elastodynamic equations, in the transient regime, in a heterogeneous and anisotropic medium [10,11]. In polycrystalline materials, the main contribution to the ultrasonic attenuation, rarely taken into account in the modelling, is that of the scattering of the wave by the microstructure. The ultrasonic wave attenuation is modelled in the ATHENA code through addition of an imaginary part to the elastic constants (equivalent viscoelastic medium). It allows taking attenuation into account as a function of the direction of

propagation versus anisotropy [12,13] and the measured values were validated by comparison with experimental and theoretical data from the literature [14,15]. Provided attenuation allows the use of descriptors increasingly rich in information based on the ultrasonic amplitude, allowing better comparison between experimental and simulated data.

The simulation requires a realistic description of the weld as input data. The models of grain structure at the macroscopic scale often use simplified symmetrical descriptions [4]. Chassignole [16] defined a realistic description of the weld as large domains in which the average orientation of the grains is obtained by macrographic analysis, but this implies a calibrated workpiece representative of the part. Grain-scale modelling (grain width is about one hundred microns) is possible [17,18] but requires as input data grain size distribution and local crystallographic orientations (which can be estimated by EBSD analysis). The LMA has developed a welding model named MINA (Modeling anIsotropy from Notebook of Arc welding) [19], which provides the microstructure of a weld, with no need for cutting. This model, created for shielded metal arc welding in flat position, allows good prediction of the grain orientation [6,20–22]. It uses information from the welding notebook (describing the welding procedure), and the rules related to crystal growth and specific welding process parameters. The elastic constants are then assigned to these orientations and the modelling of ultrasonic propagation can be performed.

Further work in the laboratory has been oriented towards the understanding of certain discrepancies occurring between modelling and experimentation. When the MINA-ATHENA coupling is used, in an inversion process, to refine the description of the microstructure of a weld [23], or to retrieve the order of passes (first order parameter in the MINA model) [24] which would not be indicated in the welding notebook, the

inversion algorithm may not converge because of the differences between the model and the experimental measures. Similarly, when grain orientations are extracted from the macrograph, the coupling with ATHENA also results in some differences.

ATHENA as all simulation codes uses as input data the description of the weld, and the elastic constants Cij, for which experimental measurements on calibrated workpieces have shown they have a certain variability. How this variability affects the simulation results is studied in this paper.

The method of analytical uncertainty propagation is applied. This method makes it possible to determine the influence of each Cij uncertainty on the simulation result. The parametric descriptor used is the seismogram, which is a representation in the {space; time} domain, corresponding to the signals recorded in each receiving point at the surface of the part. The analytical uncertainty propagation approach, under condition of linearity, is perfectly competitive with the Monte-Carlo approach, since the latter requires a much longer calculation time, given the number of random variables to simulate. Indeed the Athena model used in this study presents 4 freedom degrees. According to central limit theorem an acceptable evaluation of the uncertainties requires thousands of simulations with Monte-Carlo approach. It is a good solution for an accurate study of a particular configuration, but it is a heavy one if the goal is to prepare NDT and check multiple configurations.

The configuration that has been selected for inversion is chosen as starting configuration, because of its great sensitivity to the highly dissymmetric orientations present in the weld, here a horizontal position weld (horizontal welding of two vertical pieces) and a T60 testing beam (transverse waves at 60°).

The consequences of Cij uncertainty are discussed in terms of Non-Destructive Testing, in particular how it influences the position and the time of flight of the amplitude maximum according to the position of the transducers.

2. MODELLING OF ULTRASOUND PROPAGATION THROUGH ANISOTROPIC HETEROGENEOUS WELDS. CONFRONTATION WITH EXPERIMENTAL DATA

2.1 Propagation modelling

The heterogeneous and anisotropic weld is described in ATHENA by a finite number of homogeneous orthotropic domains (meshes). Each domain has its own local grain orientation, so that the propagation code can deduce the orientation of the coordinate systems of the elastic constants in each point of the weld. Required parameters are then:

- the elastic constants of the medium (Cij). Elastic constants of austenitic stainless steel welds have been the subject of dedicated research [16,25].
- the orientation of the coordinate systems of the elastic constants, which corresponds to the mean orientation of the grains within the defined domain.

The weld selected for this study is an austenitic stainless steel multi-pass weld made by a manual process of shielded metal arc welding, in horizontal position (that is to say, horizontal welding of two vertical pieces). The adaptations that the use of the MINA model requires in this case have still not been validated. Here, the orientation of the grains in the weld (see Figure 1b below) is thus obtained from macrographic analysis.

In order to obtain the Cij values, seven homogeneous, orthotropic samples with different grain orientations (from 0° to 90°, 15° increment) were cut out from a weld mockup. The tensor of the elastic constants of homogeneous orthotropic materials is

composed of 9 independent elastic constants (Table 1). They were determined [26] from a measurement of velocities associated with an optimization algorithm in the framework of a previous project ANR MOSAICS [27].

	Elastic constants (GPa)								
	C11	C22	C33	C23	C13	C12	C44	C55	C66
mean	230.9	256.7	242.9	131.1	142.9	143.6	64.7	110.0	111.0
mini	217	254	230	123	134	140	54	98	110
maxi	236	258	283	135	153	154	69	130	113

Table 1. Elasticity constants of the welded metal (austenitic stainless steel), where the axis of crystallographic texture <100> corresponds to axis 1 [26]

In the hypothesis of a 2D problem, with ultrasonic wave propagation in the symmetry plane (1,3), only the four values of elastic constants C11, C33, C13 et C55 are taken into account in the ATHENA modelling.

2.2 Experimental configuration and comparison with modelling

In order to get closer to industrial conditions, single side tandem in reflection mode was used (Figure 1a). A single element transducer, 7.7mm in diameter, mounted on a variable-incidence perspex wedge, and tuned to generate transverse waves with a propagation angle of 60° (T60) in the base metal, was chosen for the emission. A linear array, 2.25 MHz frequency, consisting of 64 elements with a pitch of 2.05 mm, that is, reception over about 130 mm (no delay law, element by element listening), was chosen for the reception. The advantage of being able to achieve reception over a long distance

is that the appreciation of the profile of the ultrasound beam after its crossing through the weld (notably, visualization of the beam division and deviation phenomena) is made possible without moving the receiver. This ensures a constant coupling. A series of tests conducted within the frame of the ANR MOSAICS project has shown that the T60 acquisition, compared with L0 and T45, was of great interest for this work, as it is highly sensitive to the orientations of the grains in the horizontal weld studied (Figure 1b).

Acquisitions are made with mechanical displacement of the emitter/receiver pair (fixed relative to each other) every 10 mm in the base metal, and then every 5 mm as soon as the beam reaches the weld, totalling 36 positions (Figure 1c).

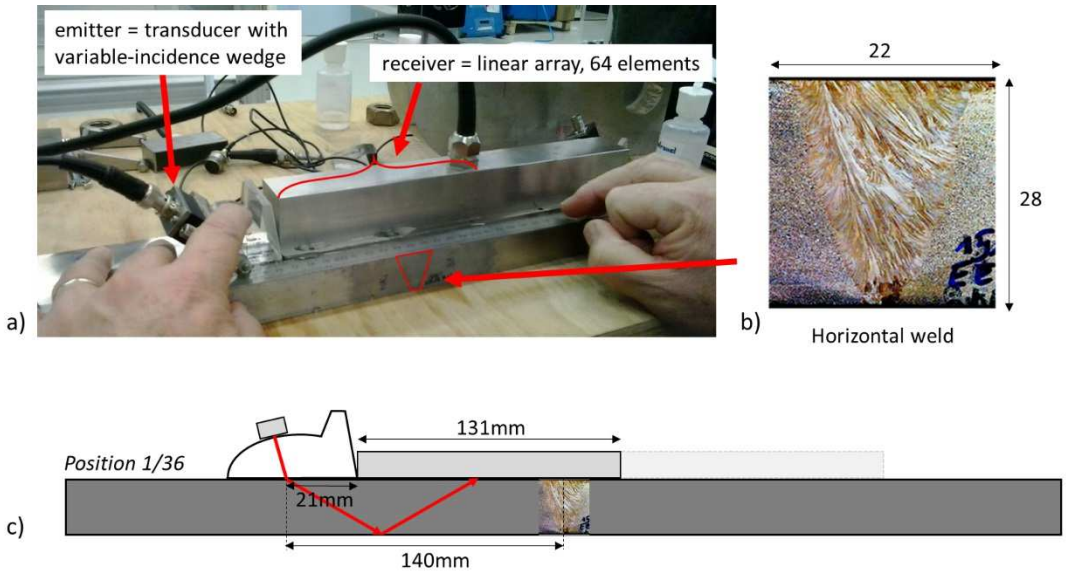

Figure 1. Experimental testing procedure; a) tandem mode; b) macrograph of the multi-pass horizontal weld (h 28mm x l 22mm, 27 passes on 10 different layers); c) principle diagram of tandem mode testing (e.g. position P140, where emitter is at 140mm from the center axis of the weld)

198 Figure 2 represents the “beam tracing” which is actually the norm of maximum velocity
199 reached at each node of the mesh during the FEM simulation. This representation amounts
200 more or less to plot the energy propagation and makes it easier to visualize the ultrasonic
201 propagation (especially deviations and divisions) inside the part. Given the central
202 frequency of the ultrasonic beam (2.25 MHz) and the velocity of the shear wave in steel
203 (about 3200 m/s), the wavelength in the weld is about 1.5 mm. The size of the mesh in
204 ATHENA - which must be at most equal to one-twelfth of the wavelength - is taken equal
205 to 0.1mm. Figure 2 shows perfectly the disturbances of the ultrasonic beam through a
206 heterogeneous anisotropic weld.
207

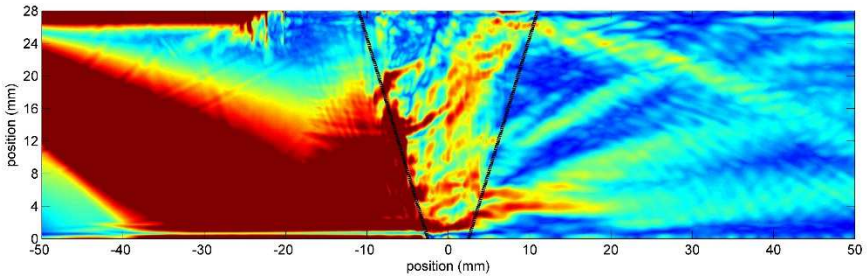

208

209 Figure 2. Energy propagation in the horizontal weld for the position of the transmitter
210 70mm from the centre axis of the weld (P70). Image deliberately saturated to enhance
211 contrast in the area of interest
212

213 The surface waves generated by the 2D simulation (visible on the left of the surface)
214 are highly numerically amplified compared with the actual 3D case. In the configuration
215 used in our study, these waves arrive at the receiver elements almost at the same time as
216 the T60 waves reflected on the bottom of the piece. Three flat defects were then artificially
217 positioned on the entry surface (at abscissa about -20mm) to block those surface waves.

The maximum of received amplitude over the whole receiving elements is registered for each position of the tandem transducers. This type of preliminary result enables observing mainly the deviation (and attenuation too) undergone by the beam during the propagation through the weld. The comparison between the modelled and experimental values is shown in Figure 3. There is a good overall agreement. The mean relative error is less than 20%, and the same general trends can be found.

The remaining amplitude discrepancies between model and experience can be partly accounted for by the fact that contact coupling remains difficult to keep constant between the sensors and the piece, for all the positions of the emitter-receiver set. In particular, it can be seen that the experimental amplitudes beyond the 20mm abscissa, unlike the simulated ones, do not regain their initial height (between -140mm and -120mm) while again propagation occurs in the base metal only.

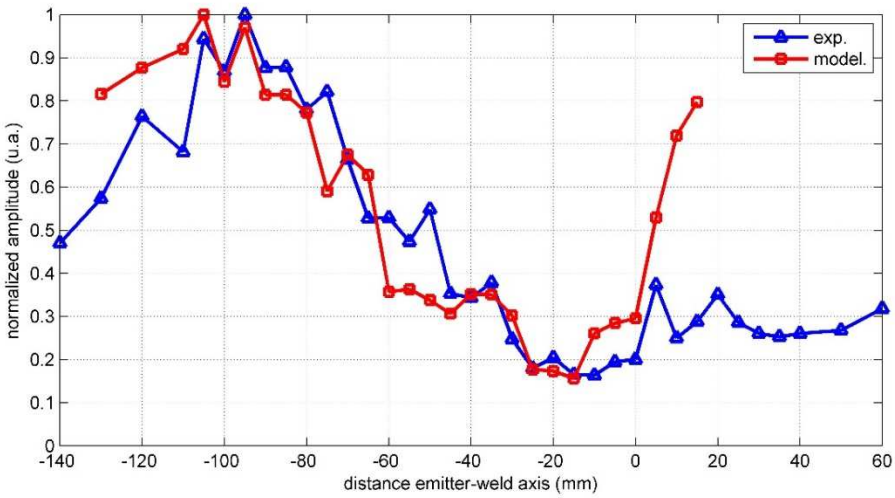

Figure 3. Maximum amplitude received over the whole receiving elements, as a function of the position of the emitter. Simulated and experimental results

Discrepancies can also be explained by considering the elastic constants Cij and their uncertainties. This idea emerged when the MOSAICS project [27] was nearly completed and has been used by Rupin et al [34], which confirm this influence in a context of defect detection (side drilled hole and notch), according a fixed test configuration (L45). As for us, we have chosen to study the influence of the Cij uncertainty on the whole ultrasonic propagation in a weld, in various testing configurations (T60, T45, L45…), using the analytical uncertainty propagation method. This work has been carried out within the frame of the ANR MUSCAD project.

3. ANALYSIS OF THE INFLUENCE OF THE ELASTIC CONSTANT UNCERTAINTY ON ULTRASONONIC PROPAGATION IN A WELD

3.1 Introduction

Elastic constants are of the utmost importance for the numerical simulation of wave propagation. In our case, they were obtained from a series of measures of longitudinal and transverse wave phase velocities, for numerous incidences and in numerous planes of incidence, combined with an optimization algorithm [25,26]. Let us recall that only four elastic constants are to be considered in the case of a 2D problem. Measurements of the Cij values were performed 7 times, once per sample exhibiting a particular homogeneous grain orientation (Figure 4). These measurements show a variability that can be great (Table 2).

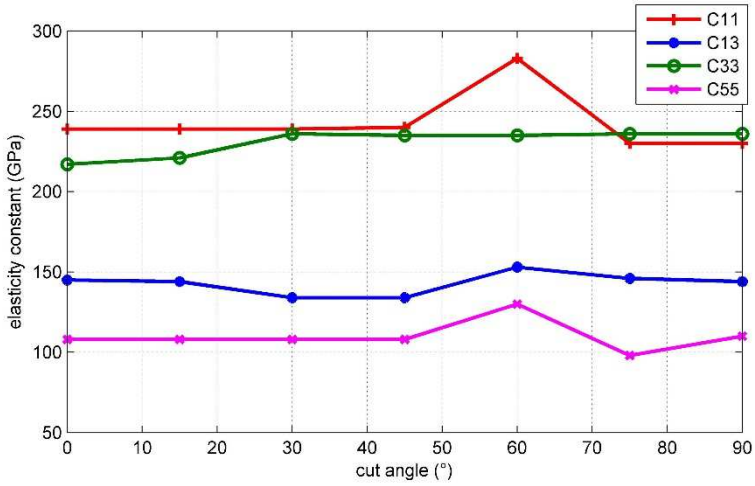

Figure 4. Elastic constants measured on 7 homogeneous orthotropic samples as a function of the cut angle with respect to the grain elongation axis in the sample (measurements of LVA INSA Lyon, ANR MOSAICS)

	C11	C33	C13	C55
mean (GPa)	242,9	230,9	142,9	110,0
mini (GPa)	230	217	134	98
maxi (GPa)	283	236	153	130
standard deviation σ_{Cij} (GPa)	18	8	6	5,5

Table 2. Elastic constants expressed in the appropriate 2D coordinate system for ATHENA (axis 3 corresponds to the grain elongation axis)

The method of analytical propagation of uncertainties is used here to study the simulation sensitivity to the uncertainties of the Cij. For a given position of the transmitter and a given acquisition mode (T60), this method makes it possible to determine, in a defined domain of the weld, the influence of the uncertainty of the Cij on the result of the simulation. The analytical uncertainty propagation method makes it possible to test a great

number of possible acquisition configurations (acquisition mode, position of the transmitter, descriptor) in a short space of time (unlike a method of the Monte Carlo type for example).

3.2 Method of analytical propagation of uncertainties

It is proposed to apply a method of analytical propagation of the variances [35] of measurement of the elastic constants Cij to the simulation results. This method is based on several hypotheses, among which the main one is the hypothesis of linearity of the chosen parametric descriptor with respect to the variations of the Cij. Attempts will thus be made to identify and formalize a descriptor that obeys this hypothesis.

The parametric descriptor selected here is the amplitudes of the seismogram (cf. schematic diagram of Figure 5 and example on Figure 7). A seismogram is like a Bscan representation, in the {space; time} domain, but corresponding to the time signals recorded by each element in the linear receiver array (the transducer does not act as a transmitter/receiver and does not move, unlike the Bscan case). From the seismogram, it is possible to extract numerous information, such as the amplitude (e.g., the maximum amplitude), the time of flight (associated with the maximum amplitude for example) as well as the deviation (discrepancy between the actual arrival position of the maximum amplitude and the theoretical one for example).

The raw seismogram supplied by ATHENA is the set of time signals received in each point of the surface. The amplitude sensitivity to the Cij is studied. A Hilbert transform is applied on the time axis to obtain the envelope of the signals, and a 2D Gaussian filter is used aiming at smoothing the numerical artefact phenomena.

In order to provide clarity for the theoretical developments presented, it is decided to use as notation for the Cij the vector c_i with i ranging between 1 and 4, for which c_1 = C11, c_2 = C33, c_3 = C13 et c_4 = C55. Each c_i being measured 7 times experimentally, the term c_{i_k} will represent the kth measure of c_i.

Let S be the seismogram expressed as a matrix $S = [s_{nm}]$ where s_{nm} corresponds to the amplitude of a point (x,t) on the seismogram. The number of points along the space axis x, given a 0.1 mm mesh and 160 mm acquisition (capturing the whole surface of the piece), is equal to 1600. The number of points along the time axis t, given the 0.016225 µs increment imposed by ATHENA and 60 µs acquisition duration, is equal to 3697. Each seismogram thus corresponds to a matrix of about 5 million points.

The analytical uncertainty propagation equation indicates that the variances of the simulation results are equal to the product of the gradients representing the sensitivities of the model to the Cij and the covariance matrix of the Cij:

$$\sigma_{s_{nm}}{}^2 = \sum_{i=1}^{4} \sum_{j=1}^{4} \frac{\partial s_{nm}}{\partial c_i} \frac{\partial s_{nm}}{\partial c_j} \, cov\,(c_i, c_j) \quad (1)$$

$$\text{with } cov\,(c_i, c_j) = \sum_{k=1}^{nb} \frac{\left(\bar{c}_i - c_{i_k}\right)\left(\bar{c}_j - c_{j_k}\right)}{nb-1} \quad (2)$$

where nb is the number of experimental measures.

The method includes three notions (cf. Figure 5):

- the covariance matrix of the measured Cij,
- the gradients of the amplitudes of the simulated seismogram depending on each Cij (sensitivity maps),
- the variances of the amplitudes of the simulated seismogram (uncertainty map).

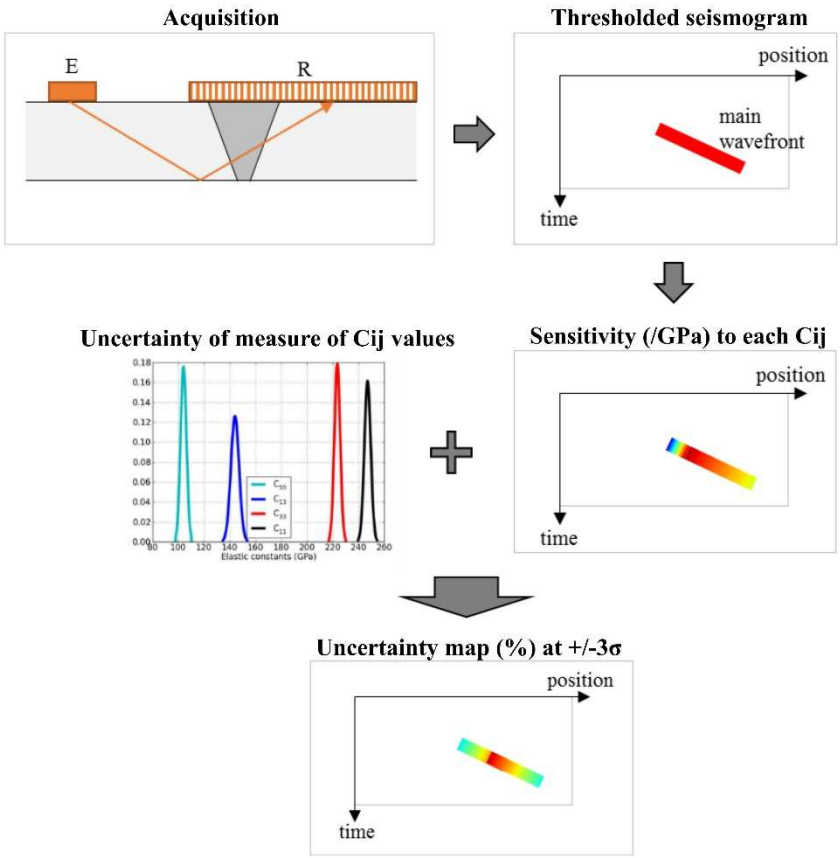

Figure 5. Schematic diagram of the method principle

3.2.1 Calculation of the covariance matrix of the Cij

The covariance matrix of the Cij is calculated from the experimental measures (cf. Figure 4). For instance, the variance of C11 is obtained as follows:

$$Var(c_1) = \sum_{k=1}^{nb} \frac{\left(\overline{c_1} - c_{1_k}\right)^2}{nb-1} \quad (3)$$

The covariance between C11 and C33 is calculated from equation 2, so that:

$$Cov(c_1, c_2) = \sum_{k=1}^{nb} \frac{\left(\overline{c_1} - c_{1_k}\right)\left(\overline{c_2} - c_{2_k}\right)}{nb-1} \quad (4)$$

The complete variance-covariance matrix is constructed under the form:

$$Cov(c_i, c_j) = \begin{bmatrix} Var(c_1) & Cov(c_1,c_2) & Cov(c_1,c_3) & Cov(c_1,c_4) \\ Cov(c_1,c_2) & Var(c_2) & Cov(c_2,c_3) & Cov(c_2,c_4) \\ Cov(c_1,c_3) & Cov(c_2,c_3) & Var(c_3) & Cov(c_3,c_4) \\ Cov(c_1,c_4) & Cov(c_2,c_4) & Cov(c_3,c_4) & Var(c_4) \end{bmatrix}$$

$$= \begin{bmatrix} 332{,}5 & 15{,}6 & -16{,}1 & -32{,}2 \\ 15{,}6 & 67{,}1 & -50{,}4 & 32{,}1 \\ -16{,}1 & -50{,}4 & 38 & -23{,}6 \\ -32{,}2 & 32{,}1 & -23{,}6 & 30{,}6 \end{bmatrix} \quad (5)$$

It is to be noted that the absolute values of covariance are quite high, particularly between c_2 and c_3, that is to say, between C33 and C13, which means that they are correlated. It is thus important these correlations be taken into account in assessing the model sensitivity to the Cij.

3.2.2 Creation of the maps of sensitivities to the Cij

The analytical uncertainty propagation method is based on the hypothesis that the modification of the simulation results is linear with respect to the variations of the Cij (Figure 6a). Thus in each point of the seismogram, one must check the linearity of the amplitude depending on each Cij. The linearity results are plotted and discussed below in the "results" paragraph, and an example of the principle is given here for C11, for a given point on the seismogram, within a variation range for C11 of ± 20GPa (Figure 6b).

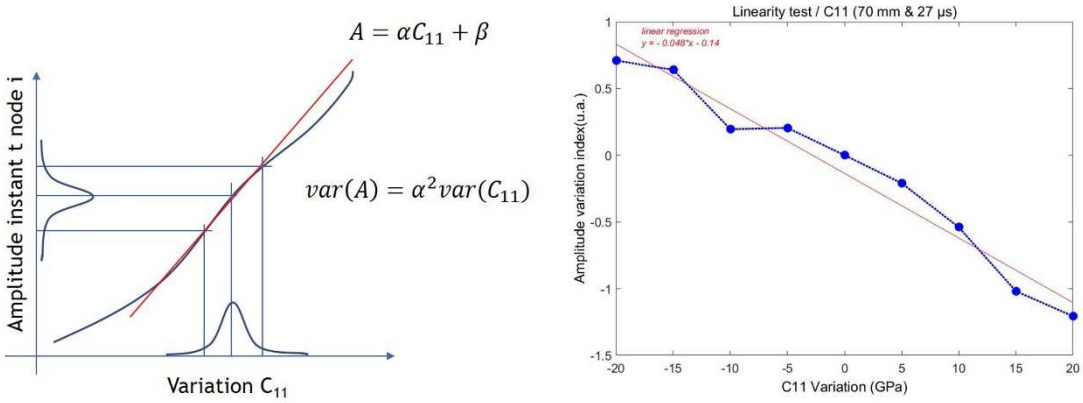

Figure 6. a) Linearization for the analytical propagation of uncertainties b) Example of a linearity test for C11 (x = 70mm and t = 27µs on the seismogram)

The sensitivity to a given Cij corresponds to the partial derivative of the amplitude of each point on the seismogram with respect to this Cij (cf. equation 1). The slope α of the linear regression line (see example of Figure 6b) corresponds to the sensitivity. For each point on the seismogram, a sensitivity to a particular Cij is thus calculated, and is represented, in the same system (x,t), in the form of a sensitivity map.

3.2.3 Creation of the map of uncertainties due to the variations of the Cij

Multiplying model sensitivities to the Cij by the variance-covariance matrix of the Cij, one obtains the variances of the simulation results (equation 1), which are represented under the form of an uncertainty map. The uncertainty corresponds to the containment of the possible error on the simulated ultrasonic amplitude. It is calculated according to the equation:

$$uncertainty(x,t) = \pm 3 \cdot \sqrt{{\sigma_{S_{nm}}}^2} \quad (6)$$

Thanks to the use of the uncertainty analytical propagation model, a complete study of a test configuration requires 37 simulations. A first simulation is carried out using the mean Cij estimates. This simulation serves as a reference for the study of the simulation variations. For each of the 4 Cij, 9 simulations are then performed, with a variation of the Cij centered on the average Cij and in a variation range of the same order of magnitude as the range observed experimentally. These 9 simulations make it possible to study the sensitivity of the simulation results, as well as verify the linearity assumption. The exploitation of these 9 simulations will be represented on Figure 9.

The simulations are parallelizable, making the method viable, from the perspective of the calculation time, for the preparation of test configurations on demand. In comparison, a similar study with the Monte-Carlo method requires several thousands of simulations, but this latter makes it possible to forget about statistical assumptions such as the linearity of the simulation result with respect to the Cij variations.

3.3 Results

Figure 7 shows the seismogram associated with the simulation of the test configuration where the emitter is positioned at P70 (position in Figure 7). The numerical « listening » (i.e., reception) is done on the whole surface of the part. Thus the seismogram is composed of 2 different zones. Zone 1 is not accessible experimentally. It is possible to visualize the emission as well as the surface waves and their reflection by the “numerical cracks” (notches). Zone 2 is the region of interest, where the ultrasonic waves are received after passing through the weld. In the following, the results will be plotted only in this zone. Figure 7 emphasises again that passage through the weld causes splitting, skewing and attenuation of the ultrasonic beam.

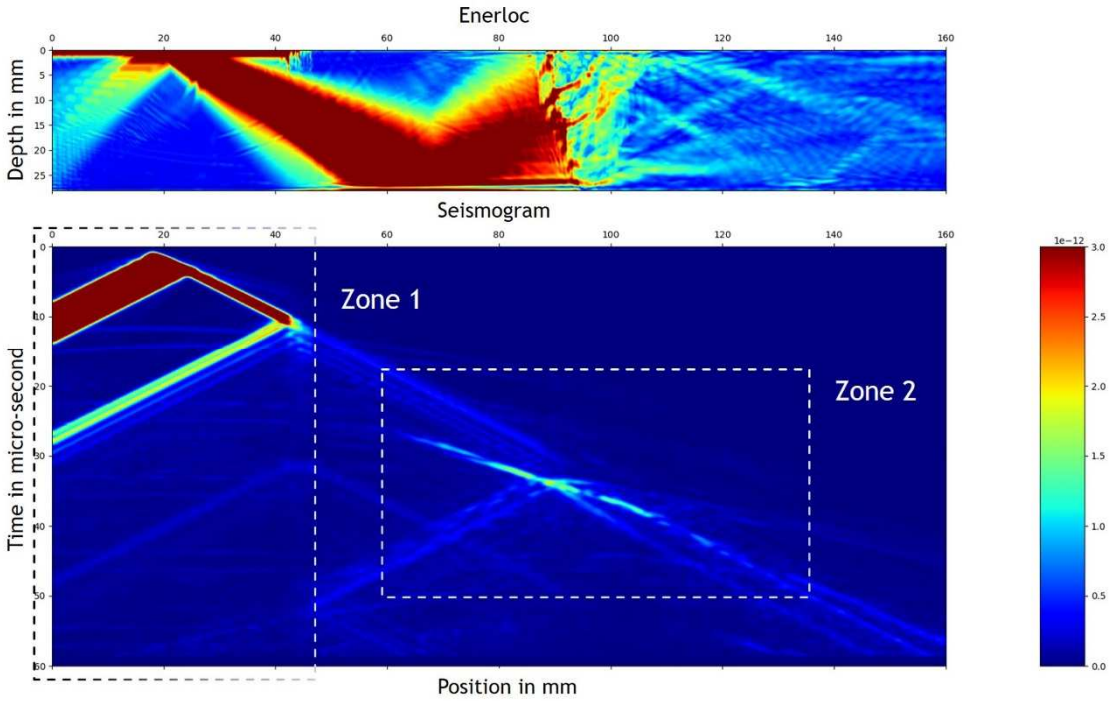

Figure 7. Ultrasonic propagation and seismogram for configuration T60 and position P70 of the emitter. Images voluntarily saturated to enhance propagation through weld

In the section 3.2.2 the hypothesis of linearity has been made. The linearity of simulation results against Cij variations is the condition to obtain a Gaussian probability density function (pdf) of the error. If a non-linearity is present, this can induce a deformation of this function. It is important to check the linearity to detect potential bias in the uncertainties evaluation. It has been shown that the sensitivity is estimated by the slope of a linear regression. The residues' variance of the linear regression is compared to the residues' variance of a quadratic regression. If the two variances are close, it means that the quadratic regression and the linear one are equivalent. The linear regression is then sufficient. The linearity index is considered as the ratio of the two variances, and a

399 Fisher test is applied on this linearity index. A linearity index below the α-risk of 5%
400 means that the probability that the linearity assumption is respected becomes low.
401 Figure 8a represents the echodynamic curve, which corresponds to the maximum of
402 amplitude received at each point on the surface of the part (maxima of seismogram
403 columns). And Figure 8b shows the linearity index along the echodynamic curve. The
404 condition of linearity for the whole Cij is respected at the beginning of the main echo
405 from 70 mm to about 88 mm. That means that in this region the uncertainties are well
406 estimated. In the next zone mostly the linearity of C13 exceeds the α-risk of 5% threshold.
407 Thus the error bar, which is usually centered on the mean value of the seismogram
408 amplitudes considering a gaussian pdf, can lose its symmetry and be decentered. This
409 region must be then considered with caution, as well as an area that would be linear but
410 with a large standard deviation.
411

412 a)

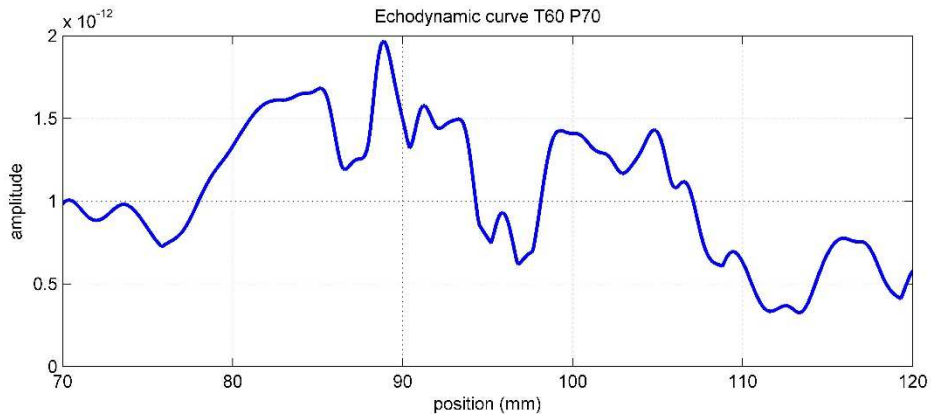

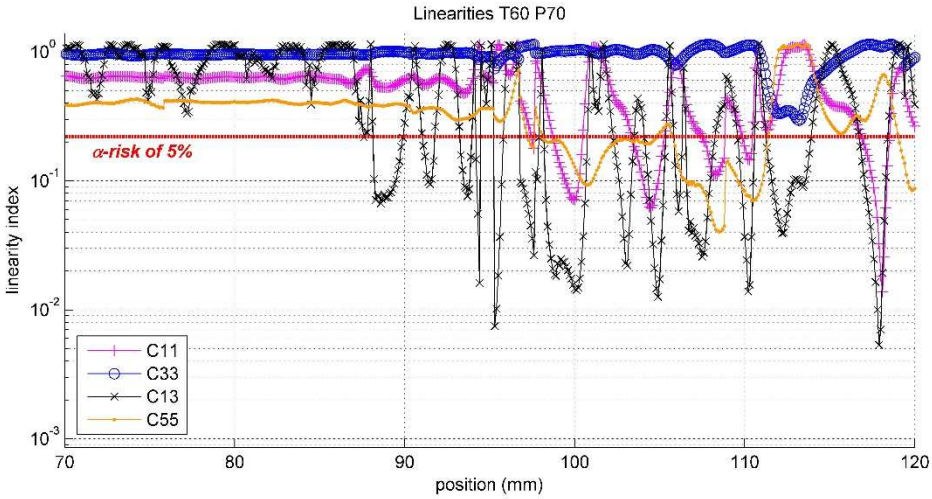

b)

Figure 8. a) Echodynamic curve drawn in the region of interest zone 2, from position 70 to 120 mm b) Linearity index of the echodynamic points, for configuration T60 and position P70 of the emitter

The maps of sensitivities to the elastic constants are shown Figure 9. They were calculated for Cij variations of $\pm \sigma_{Cij}$ listed in Table 2, and plotted in the coordinate system of the seismogram. Also, the value of the standard deviation (calculated from the Cij variances, cf. equation 3) is indicated for each Cij.

To facilitate the analysis, the initial sensitivity map was processed: the seismogram was segmented so that only the points on the image corresponding to the main wavefront appear, and it was chosen to keep on the image only the main wavefront sensitivities.

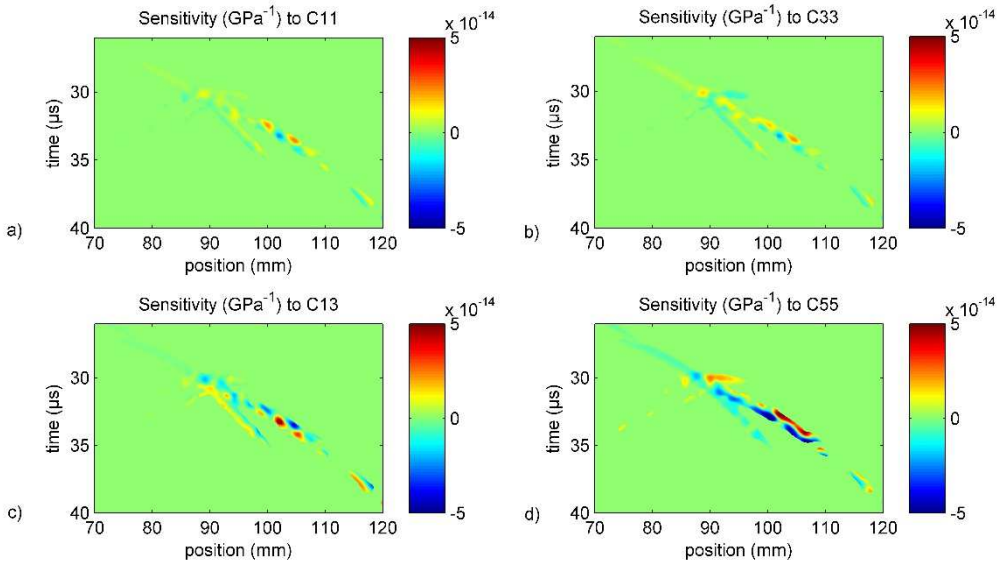

426

427 Figure 9. Maps of the amplitude sensitivities (GPa^{-1}) to the Cij (Cij variation from -

428 σ_{Cij} to $+\sigma_{Cij}$ of Table 2, T60, P70)

429

430 The map of the amplitude uncertainties due to the variations of the elastic constants

431 (Figure 10) gives the influence of the variation of all the Cij simultaneously, this time

432 taking into account their standard deviations. Each point in the map has an uncertainty

433 corresponding to the possible simulated amplitude error containment.

434 As in the case of the sensitivities, in order to facilitate the analysis the initial map of

435 uncertainties was processed: it was chosen to keep on the image only the main wavefront

436 uncertainties.

437

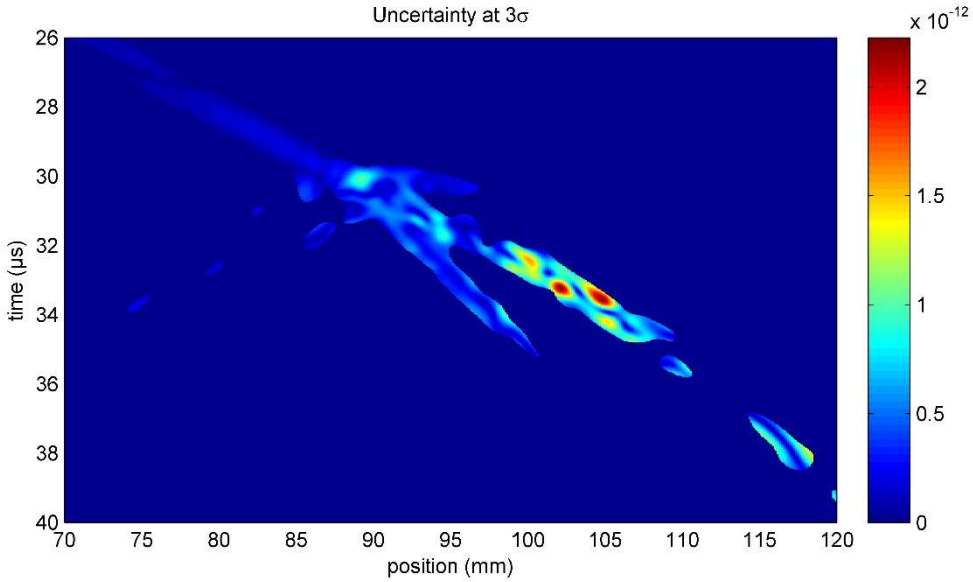

Figure 10. Map of amplitude uncertainties due to the variations of Cij (T60, P70)

Figure 11 shows the echodynamic curve in blue, surrounded by the corresponding uncertainties at $\pm 3\sigma$ (red and green curves) extracted from Figure 10. The zone of the echodynamic curve comprised between 70 and 85 mm corresponds to a surface wave generated by reflection on the weld bead. As this surface wave propagates mainly in the base metal, it is only hardly influenced by the weld. On the abscissa from 90 to 100 mm, the echodynamic curve presents a high amplitude and a quite low uncertainty. From this observation it is possible to highlight a more reliable zone for a NDT test in this configuration. Conversely, the zones situated beyond 100 mm show a higher uncertainty, and should therefore be avoided.

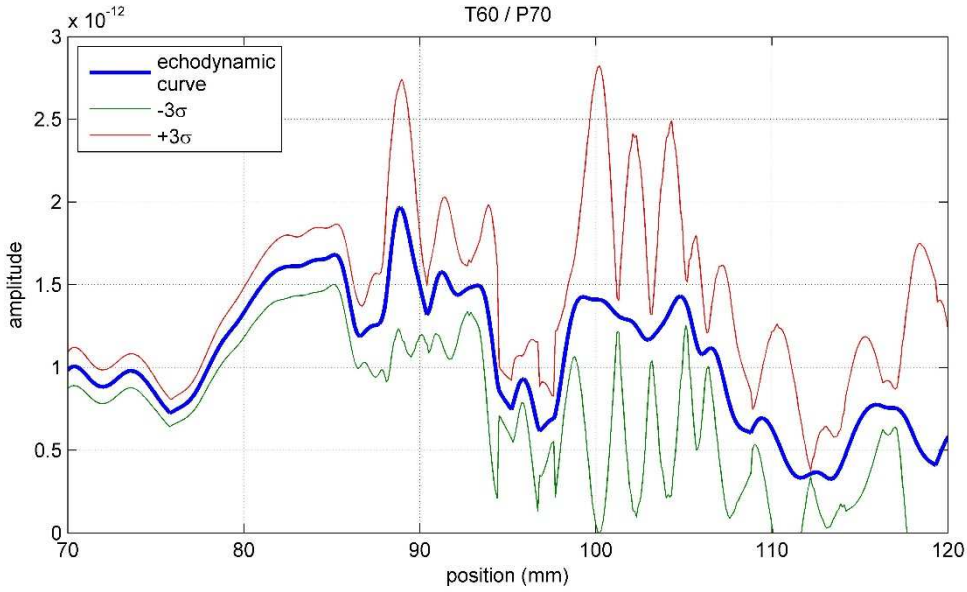

Figure 11. Result in terms of echodynamic curve (T60, P70) and associated uncertainty at $\pm 3\sigma$

Results showed that for the chosen test configuration (T60, emitter in position P70), Cij uncertainties have a certain impact on the simulation results. It should be noted that the chosen configuration is quite favourable, the ultrasound beam being reflected first on the bottom of the part before passing through the weld. The Cij variation has little effect on the ultrasonic propagation, as propagation after the weld is short, which limits the effects of beam deviation and division caused by the weld.

Simulation tests, still in T60, but for a new emitter position (P30) were carried out (Figure 12). The ultrasonic beam passes through the weld before being reflected on the bottom of the part. The same calculations are performed, with the same uncertainties on the Cij as before.

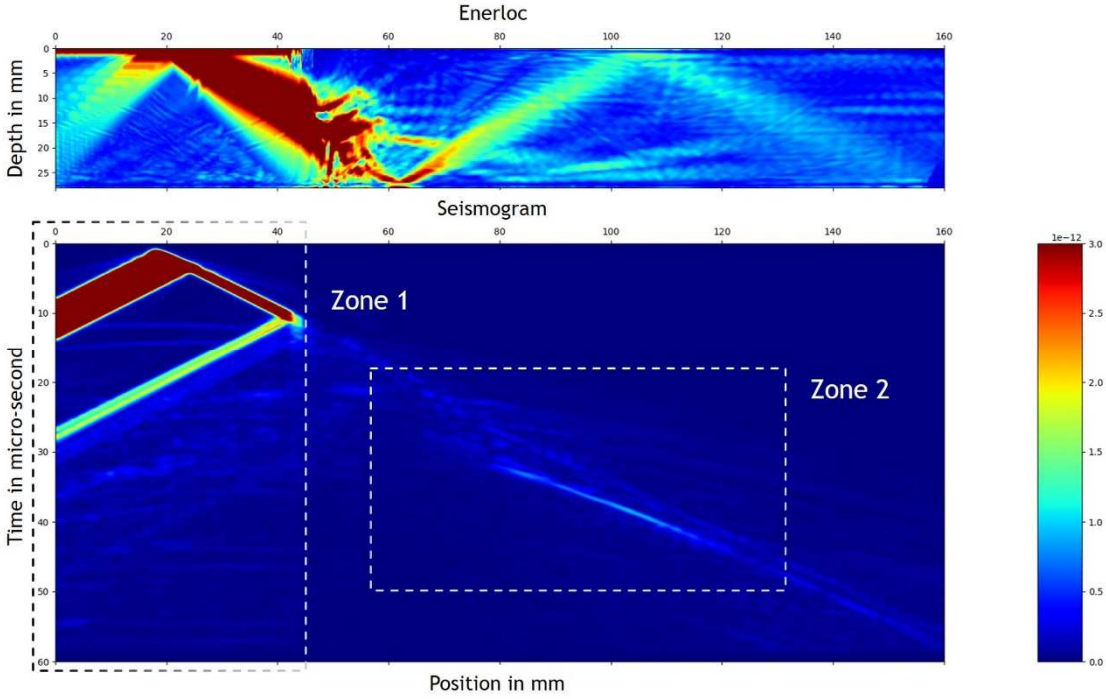

Figure 12. Ultrasonic propagation and seismogram for configuration T60 and position P30. Images voluntarily saturated to enhance propagation through weld

The uncertainty associated with the echodynamic curve in Figure 13 is on average largely greater than the uncertainties observed in Figure 11. This increase can be accounted for by the fact that, on the one hand, ultrasound pass through the weld differently from the previous configuration, and, on the other hand, the distance covered in the base metal beyond the weld is much greater, amplifying the modifications of the propagation occurring in the weld when the Cij vary. However, at positions 85-90 mm and 105-110 mm, two narrow stabilization zones appear. The analytical propagation method allows identification of these two zones as being reliable control areas, hardly sensitive to the Cij variations.

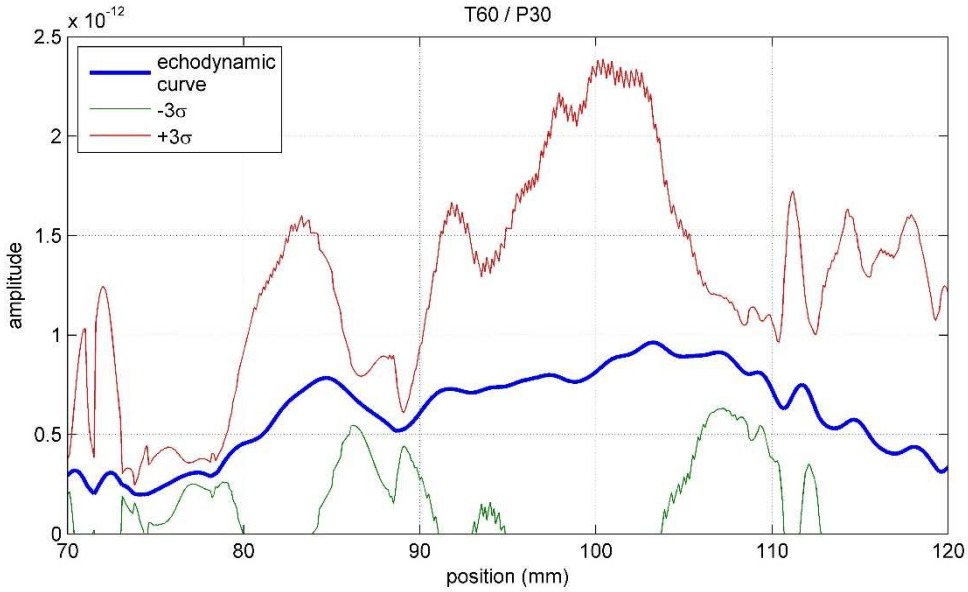

Figure 13. Result in terms of echodynamic curve and associated uncertainty at $\pm 3\sigma$ (T60, P30)

3.4 Discussion on the consequences for NDT

In conventional industrial NDT, the location of a detected defect, its nature and its dimensions, can be obtained by studying the propagated acoustic beam. The procedures are different depending on whether a pulse-echo mode or a tandem mode is used, but the principle remains the same: the position of the maximum ultrasonic amplitude is sought. This position corresponds to the theoretical axis of the propagated beam if there is no deviation of the beam (isotropic material), and if the input data in terms of ultrasonic velocity are those of the material. Otherwise, there will be a gap between the theory and the experiment that prevents a reliable control result. Confidence in the control performed can be given if one is able to relate this deviation of the beam to the characteristics of anisotropy and heterogeneity of the material. It is therefore necessary that these latter are perfectly known.

Our study shows that the uncertainty about the knowledge of these characteristics, therefore of the Cij, not only has a negative consequence on the control simulations of a weld, but also that this consequence is different according to the controlled weld zones.

Focusing on the maximum amplitude point of the main wavefront on the seismogram, for position P70 (Figure 7), the displacement of this maximum point in position ($disp_x$) and in time ($disp_t$), caused by the variation of each Cij, can be noted. The results obtained are presented in Table 3 and they show that for this control position, the uncertainty on the Cij has practically no effect on the simulated results.

Displacements of the maximum amplitude point				
	C11	C33	C13	C55
$disp_x$ (mm)	0	0	0.1	0.1
$disp_t$ (µs)	0.05	0.03	0.03	0.02

Table 3. Displacements in position and in time of the maximum amplitude point of the main wavefront (Cij variation from $-\sigma_{Cij}$ to $+\sigma_{Cij}$ of Table 2, T60, P70)

However for position P30 (seismogram of Figure 12), we show that the displacements, in position and in time, of the maximum amplitude point of the main wavefront are, for this control configuration, far greater (Table 4). The variation of a Cij can cause a significant displacement of the echo (for example here, about 8 mm and 2.5 µs) and thereby lead to false NDT diagnosis. Indeed, a deviation greater than 2-3 mm in the position of the amplitude maximum and/or a difference of 1 µs are sufficient to disturb the controller. He/she no longer understands the propagation of the beam, and he/she can't

reliably decide for example if an echo corresponds to a defect or to a specific geometry of the sample.

Displacements of the maximum amplitude point				
	C11	C33	C13	C55
$disp_x$ (mm)	8.3	4.1	3.9	0.7
$disp_t$ (µs)	2.56	1.25	1.25	0.26

Table 4. Displacements in position and time of the maximum amplitude point of the main wavefront (Cij variation from $-\sigma_{Cij}$ to $+\sigma_{Cij}$ of Table 2, T60, P30)

4. CONCLUSION AND PERSPECTIVES

Among the various parameters that may affect modelling of the non-destructive testing of a multi-pass weld, we have identified the uncertainty on the values of Cij, which are critical input parameters for any ultrasonic propagation simulation code.

On the one hand, they are difficult to evaluate experimentally, and on the other hand the samples on which the measurements are performed may not be representative of the welded metal.

This study has made it possible to quantify the influence of the precise knowledge of the Cij on the ultrasonic propagation simulation, this influence being highly dependent on the testing conditions (position of the sensors relative to the weld). It has clearly demonstrated that conventional non-destructive testing (consisting of searching the evolution for echo maxima) will be influenced and disturbed by the beam deviation, and the change in time of flight. The only way to reduce this disturbance is the most precise knowledge possible of Cij. This can be done through a specific characterization procedure

of the controlled materials. But here we show the limits obtained when, in industrial condition, we use a database of Cij recorded for a wide range of materials. Indeed elasticity constants generally used are taken from the literature and they are not exactly in accordance with those of the tested specimen.

Choosing the seismogram as descriptor makes it possible to keep the maximum amount of information. Its association with the sensitivity and uncertainty maps reveals the zones that are sensitive (or not) to the variations of each Cij. This can help in the choice of the best experimental configurations, whether for testing or for determining, through an inversion process, the properties of the weld structure (e.g., the grain orientations). This experimental phase of in-situ weld characterization should thus precede the ultrasonic testing itself aimed at the detection of defects.

The calculation time is significantly reduced, with 37 necessary simulations instead of several thousand for a typical Monte-Carlo method, through application of the analytical uncertainty propagation method. This will allow us to carry on with our work, studying a great number of other configurations (L45, T45, L60, other sensor positions, other welds).

Further study will be also carried out on the influence of the uncertainty of the imaginary part of the Cij, very difficult to measure, and whose effect on the modelled attenuation will be significant.

Acknowledgements

This work was realized in the framework of the MUSCAD (Méthodes UltrasonoreS pour la Caractérisation de matériaux de composants nucléaires pour l'Amélioration du Diagnostic) project which is supported by the French National Agency of Research.

References

[1] G. Corneloup, C. Gueudré, Non Destructive Testing and testability of materials and structures (Le contrôle non destructif et la contrôlabilité des matériaux et structures), PPUR, 2016.

[2] B. Chassignole, R. El Guerjouma, M.-A. Ploix, T. Fouquet, Ultrasonic and structural characterization of anisotropic austenitic stainless steel welds: Towards a higher reliability in ultrasonic non-destructive testing, NDTE Int. 43 (2010) 273–282. doi:10.1016/j.ndteint.2009.12.005.

[3] S. Wagner, S. Dugan, M. Barth, F. Schubert, B. Koehler, Welding for Testability: An Approach Aimed at Improving the Ultrasonic Testing of Thick-Walled Austenitic and Dissimilar Metal Welds, Rev. Prog. Quant. Nondestruct. Eval. Inc. 10th Int. Conf. Barkhausen Noise Micromagnetic Test. Vols 33a 33b. (2014) 1045–1052. doi:10.1063/1.4864936.

[4] J.A. Ogilvy, Computerized Ultrasonic Ray Tracing in Austenitic Steel, NDTE Int. 18 (1985) 67–77. doi:10.1016/0308-9126(85)90100-2.

[5] S.R. Kolkoori, M.-U. Rahman, P.K. Chinta, M. Ktreutzbruck, M. Rethmeier, J. Prager, Ultrasonic field profile evaluation in acoustically inhomogeneous anisotropic materials using 2D ray tracing model: Numerical and experimental comparison, Ultrasonics. 53 (2013) 396–411. doi:10.1016/j.ultras.2012.07.006.

[6] O. Nowers, D.J. Duxbury, B.W. Drinkwater, Ultrasonic array imaging through an anisotropic austenitic steel weld using an efficient ray-tracing algorithm, NDTE Int. 79 (2016) 98–108. doi:10.1016/j.ndteint.2015.12.009.

582 [7] H. Zhou, Z. Han, D. Du, Y. Chen, A combined marching and minimizing ray-tracing
583 algorithm developed for ultrasonic array imaging of austenitic welds, NDTE Int. 95
584 (2018) 45–56. doi:10.1016/j.ndteint.2018.01.008.
585 [8] P. Calmon, S. Mahaut, S. Chatillon, R. Raillon, CIVA: An expertise platform for
586 simulation and processing NDT data, Ultrasonics. 44 (2006) E975–E979.
587 doi:10.1016/j.ultras.2006.05.218.
588 [9] A. Imperiale, S. Chatillon, M. Darmon, N. Leymarie, E. Demaldent, UT Simulation
589 Using a Fully Automated 3D Hybrid Model: Application to Planar Backwall
590 Breaking Defects Inspection, Rev. Prog. Quant. Nondestruct. Eval. Vol 37. (2018)
591 1–8. doi:10.1063/1.5031546.
592 [10] E. Becache, P. Joly, C. Tsogka, An analysis of new mixed finite elements for the
593 approximation of wave propagation problems, SIAM J. Numer. Anal. 37 (2000)
594 1053–1084. doi:10.1137/S0036142998345499.
595 [11] E. Becache, P. Joly, C. Tsogka, Fictitious domains, mixed finite elements and
596 perfectly matched layers for 2-D elastic wave propagation, J. Comput. Acoust. 9
597 (2001) 1175–1201. doi:10.1142/S0218396X01000966.
598 [12] B. Chassignole, V. Duwig, M.-A. Ploix, P. Guy, R. El Guerjouma, Modelling the
599 attenuation in the ATHENA finite elements code for the ultrasonic testing of
600 austenitic stainless steel welds, Ultrasonics. 49 (2009) 653–658.
601 doi:10.1016/j.ultras.2009.04.001.
602 [13] M.-A. Ploix, P. Guy, B. Chassignole, J. Moysan, G. Corneloup, R. El Guerjouma,
603 Measurement of ultrasonic scattering attenuation in austenitic stainless steel welds:
604 Realistic input data for NDT numerical modeling, Ultrasonics. 54 (2014) 1729–
605 1736. doi:10.1016/j.ultras.2014.04.005.

606 [14] T. Seldis, C. Pecorari, Scattering-induced attenuation of an ultrasonic beam in
607 austenitic steel, J. Acoust. Soc. Am. 108 (2000) 580–587. doi:10.1121/1.429589.
608 [15] S. Ahmed, Ultrasonic Attenuation as Influenced by Elongated Grains, Rev. Prog.
609 Quant. Nondestruct. Eval. Vol 20. (2003) 109–116. doi:10.1063/1.1570126.
610 [16] B. Chassignole, D. Villard, M. Dubuget, J.C. Baboux, R. El Guerjouma,
611 Characterization of austenitic stainless steel welds for ultrasonic NDT, Rev. Prog.
612 Quant. Nondestruct. Eval. Vols 19a 19b. (2000) 1325–1332.
613 doi:10.1063/1.1307835.
614 [17] N. Feuilly, O. Dupond, B. Chassignole, J. Moysan, G. Corneloup, Relation Between
615 Ultrasonic Backscattering and Microstructure for Polycrystalline Materials, Rev.
616 Prog. Quant. Nondestruct. Eval. Vols 28a 28b. (2009) 1216.
617 doi:10.1063/1.3114093.
618 [18] P.E. Lhuillier, B. Chassignole, M. Oudaa, S.O. Kerherve, F. Rupin, T. Fouquet,
619 Investigation of the ultrasonic attenuation in anisotropic weld materials with finite
620 element modeling and grain-scale material description, Ultrasonics. 78 (2017) 40–
621 50. doi:10.1016/j.ultras.2017.03.004.
622 [19] J. Moysan, A. Apfel, G. Corneloup, B. Chassignole, Modelling the grain orientation
623 of austenitic stainless steel multipass welds to improve ultrasonic assessment of
624 structural integrity, Int. J. Press. Vessels Pip. 80 (2003) 77–85. doi:10.1016/S0308-
625 0161(03)00024-3.
626 [20] Z. Fan, M.J.S. Lowe, Investigation of Ultrasonic Array Measurements to Refine
627 Weld Maps of Austenitic Steel Welds, Rev. Prog. Quant. Nondestruct. Eval. Vols
628 31a 31b. (2012) 873–880.

[21] Z. Fan, A.F. Mark, M.J.S. Lowe, P.J. Withers, Nonintrusive Estimation of Anisotropic Stiffness Maps of Heterogeneous Steel Welds for the Improvement of Ultrasonic Array Inspection, IEEE Trans. Ultrason. Ferroelectr. Freq. Control. 62 (2015) 1530–1543. doi:10.1109/TUFFC.2015.007018.

[22] J. Moysan, C. Gueudre, M.-A. Ploix, G. Corneloup, P. Guy, R. El Guerjouma, B. Chassignole, Advances in ultrasonic testing of austenitic stainless steel welds. Towards a 3D description of the material including attenuation and optimisation by inversion, in: A. Leger, M. Deschamps (Eds.), Ultrason. Wave Propag. Non Homog. Media, Springer-Verlag Berlin, Berlin, 2009: pp. 15–24.

[23] C. Gueudre, L. Le Marrec, J. Moysan, B. Chassignole, Direct model optimisation for data inversion. Application to ultrasonic characterisation of heterogeneous welds, NDTE Int. 42 (2009) 47–55. doi:10.1016/j.ndteint.2008.07.003.

[24] C. Gueudre, L. Le Marrec, M. Chekroun, J. Moysan, B. Chassignole, G. Corneloup, Determination of the Order of Passes of an Austenitic Weld by Optimization of an Inversion Process of Ultrasound Data, Rev. Prog. Quant. Nondestruct. Eval. Vols 30a 30b. 1335 (2011) 639–646. doi:10.1063/1.3591910.

[25] P.A. Bodian, P. Guy, B. Chassignole, O. Dupont, Non-destructive evaluation of elastic properties, and ultrasonic attenuation of transverse wave of anisotropic and heterogeneous media, in: F. Bremand (Ed.), ICEM 14 14th Int. Conf. Exp. Mech. Vol 6, E D P Sciences, Cedex A, 2010: p. 36002. doi:10.1051/epjconf/20100636002.

[26] N. Alaoui-Ismaili, P. Guy, B. Chassignole, Experimental Determination of the Complex Stiffness Tensor and Euler Angles in Anisotropic Media Using Ultrasonic

652 Waves, Rev. Prog. Quant. Nondestruct. Eval. Inc. 10th Int. Conf. Barkhausen Noise
653 Micromagnetic Test. Vols 33a 33b. (2014) 934–940. doi:10.1063/1.4864921.
654 [27] B. Chassignole, P. Recolin, N. Leymarie, C. Gueudre, P. Guy, D. Elbaz, Study of
655 Ultrasonic Characterization And Propagation In Austenitic Welds: The MOSAICS
656 Project, Rev. Prog. Quant. Nondestruct. Eval. Vol 34. (2015) 1486–1495.
657 doi:10.1063/1.4914766.
658 [28] A.J. Hunter, B.W. Drinkwater, J. Zhang, P.D. Wilcox, A Study into the Effects of
659 an Austenitic Weld on Ultrasonic Array Imaging Performance, Rev. Prog. Quant.
660 Nondestruct. Eval. Vols 30a 30b. (2011) 1063–1070.
661 [29] C. Boller, S. Pudovikov, A. Bulavinov, Quantitative Ultrasonic Testing of
662 Acoustically Anisotropic Materials with Verification on Austenitic and Dissimilar
663 Weld Joints, Rev. Prog. Quant. Nondestruct. Eval. Vols 31a 31b. (2012) 881–888.
664 [30] J. Zhang, A. Hunter, B.W. Drinkwater, P.D. Wilcox, Monte Carlo Inversion of
665 Ultrasonic Array Data to Map Anisotropic Weld Properties, IEEE Trans. Ultrason.
666 Ferroelectr. Freq. Control. 59 (2012) 2487–2497. doi:10.1109/TUFFC.2012.2481.
667 [31] C. Holmes, B.W. Drinkwater, P.D. Wilcox, Post-processing of the full matrix of
668 ultrasonic transmit-receive array data for non-destructive evaluation, NDTE Int. 38
669 (2005) 701–711. doi:10.1016/j.ndteint.2005.04.002.
670 [32] L.J. Cunningham, A.J. Mulholland, K.M.M. Tant, A. Gachagan, G. Harvey, C. Bird,
671 The detection of flaws in austenitic welds using the decomposition of the time-
672 reversal operator, Proc. R. Soc. -Math. Phys. Eng. Sci. 472 (2016) 20150500.
673 doi:10.1098/rspa.2015.0500.

[33] K. Metwally, E. Lubeigt, S. Rakotonarivo, J.-F. Chaix, F. Baque, G. Gobillot, S. Mensah, Weld inspection by focused adjoint method, Ultrasonics. 83 (2018) 80–87. doi:10.1016/j.ultras.2017.08.009.

[34] F. Rupin, G. Blatman, S. Lacaze, T. Fouquet, B. Chassignole, Probabilistic approaches to compute uncertainty intervals and sensitivity factors of ultrasonic simulations of a weld inspection, Ultrasonics. 54 (2014) 1037–1046. doi:10.1016/j.ultras.2013.12.006.

[35] J. Maihle, J.M. Linares, J.M. Sprauel, The statistical gauge in geometrical verification: Part I. Field of probability of the presence of matter, Precis. Eng. 33 (2009) 333–341. doi:10.1016/j.precisioneng.2008.09.003.

685 **Collected figure captions**

686 Figure 1. Experimental testing procedure; a) tandem mode; b) macrograph of the
687 multi-pass horizontal weld (h 28mm x l 22mm, 27 passes on 10 different layers); c)
688 principle diagram of tandem mode testing (e.g. position P140, where emitter is at 140mm
689 from the center axis of the weld)

690 Figure 2. Energy propagation in the horizontal weld for the position of the transmitter
691 70mm from the centre axis of the weld (P70). Image deliberately saturated to enhance
692 contrast in the area of interest

693 Figure 3. Maximum amplitude received over the whole receiving elements, as a
694 function of the position of the emitter. Simulated and experimental results

695 Figure 4. Elastic constants measured on 7 homogeneous orthotropic samples as a
696 function of the cut angle with respect to the grain elongation axis in the sample
697 (measurements of LVA INSA Lyon, ANR MOSAICS)

698 Figure 5. Schematic diagram of the method principle

699 Figure 6. a) Linearization for the analytical propagation of uncertainties b) Example
700 of a linearity test for C11 (x = 70mm and t = 27µs on the seismogram)

701 Figure 7. Ultrasonic propagation and seismogram for configuration T60 and position
702 P70 of the emitter. Images voluntarily saturated to enhance propagation through weld

703 Figure 8. a) Echodynamic curve drawn in the region of interest zone 2, from position
704 70 to 120 mm b) Linearity index of the echodynamic points, for configuration T60 and
705 position P70 of the emitter

706 Figure 9. Maps of the amplitude sensitivities (GPa-1) to the Cij (Cij variation from -
707 σ_{Cij} to $+\sigma_{Cij}$ of Table 2, T60, P70)

708 Figure 10. Map of amplitude uncertainties due to the variations of Cij (T60, P70)

Figure 11. Result in terms of echodynamic curve (T60, P70) and associated uncertainty at $\pm 3\sigma$

Figure 12. Ultrasonic propagation and seismogram for configuration T60 and position P30. Images voluntarily saturated to enhance propagation through weld

Figure 13. Result in terms of echodynamic curve and associated uncertainty at $\pm 3\sigma$ (T60, P30)

Collected table captions

Table 1. Elasticity constants of the welded metal (austenitic stainless steel), where the axis of crystallographic texture <100> corresponds to axis 1 [26]

Table 2. Elastic constants expressed in the appropriate 2D coordinate system for ATHENA (axis 3 corresponds to the grain elongation axis)

Table 3. Displacements in position and in time of the maximum amplitude point of the main wavefront (Cij variation from $-\sigma_{Cij}$ to $+\sigma_{Cij}$ of Table 2, T60, P70)